Spalling of fire exposed concrete

B.B.G. Lottman [1], E.A.B. Koenders [3], C.B.M. Blom [2, 4], J.C. Walraven [2]

[1] Witteveen+Bos / Tunnel Engineering Consultants (TEC)

[2] Delft University of Technology, the Netherlands

[3] Technische Universität Darmstadt, Germany

[4] Municipality of Rotterdam, the Netherlands

Concrete spalling due to fire exposure is a topic that has gained a lot of attention from the scientific research community in the past decades as well as at present in the Netherlands. This destructive phenomenon is commonly characterised by a sudden and in some cases repetitive breaking off of pockets of concrete from the heated surface. Prevailing theories indicate a simultaneous action of both pore pressure and thermal stresses with their respective dominance still not yet fully understood. In this article a new multi-scale FEM-based numerical model is presented, which was derived to enable a fundamental analysis of both actions. A coupled thermal-hygral-mechanical approach is used to examine the temperature and pore pressure developments as well as the associated fracture patterns that develop in a heated concrete structural element. The simulated crack patterns indicate the occurrence of thermal instabilities at the heated concrete surface with pore pressures only adding a minor contribution. Failure is shown to occur by the progressive compression of the heated surface layer while inducing local delaminations. Finally, based on these numerical simulations and on observations from full-scale heated slabs, thermal buckling is proposed to be the main mechanism that drives concrete spalling due to fire exposure.

Key words: Concrete, fire, (explosive) spalling, pore pressure, fracture mechanics, finite element method, thermal buckling mechanism

1 Introduction

In several severe fires in especially tunnels throughout the past decades damage to the concrete structure in the form of (explosive) spalling has occurred as for instance reported by (CTSA, 1997; BEA-TT & RAIB, 2010). The need for additional research is further highlighted by current developments in the Netherlands where concrete elements, constructed and tested in accordance with the guidelines, still exhibited spalling as discussed in (Lottman, et al., 2017).

Figure 1: Spalling damage, as observed after full-scale fire testing, can be limited to the surface of the concrete slab (left) (Jansson & Boström, 2008) *or in the most severe case considerably reduce the structural capacity, as shown for a loaded tunnel lining segment (right)* (Dehn, et al., 2010)

This phenomenon is characterised by the breaking off of pieces of concrete from the heated surface with the term explosive referring to the sometimes sudden and violent occurrence (Khoury & Anderberg, 2000). Spalling can range from superficial damage to the concrete surface (Jansson & Boström, 2008) to severe damage in which the protective layer on the reinforcement is removed (Dehn, et al., 2010) as shown in figure 1. Especially the latter is, from a structural point of view, to be avoided.

In literature commonly two main theories prevail which focus either on the development of pore pressures (Harmathy, 1965) or the thermal stresses that arise from the temperature gradient (Dougill, 1972). The observed sensitivity of especially High Strength Concrete (HSC) to spalling and the found unfavourable influence of external compression loading (Khoury & Anderberg, 2000) has prompted scientific research, both experimental (RILEM TC-HTC, 2004; fib WP-4.3-1, 2007) as well as numerical (Tenchev, et al., 2001; Gawin, et al., 2003). However, both the dominance and the interaction of these main processes were at the start of the research project[1] not fully understood. The actual spalling phenomena are at the time only feasible investigated by full-scale fire tests on concrete elements (Dehn, et al., 2010). However, these efforts have not yet proven to be sufficient in identifying the mechanism.

[1] The article is based on the dissertation "The spalling mechanism of fire exposed concrete" by the first author and reports the research performed at the group Concrete Structures at Delft University of Technology, Faculty of Civil Engineering and Geosciences (Lottman, 2017)

In this article the influence of both existing theories on the development of a spalling mechanism is investigated by derivation of a conceptual Finite Element Method (FEM) based model (Lottman, 2017). This considers a fire exposed concrete structural element which is first elaborated, addressing also the adopted coupled physical and fracture mechanics approach each described by a separate FEM model. Thereafter, the definition of each FEM model is briefly discussed, reflecting on the fundamental theories, the inherent assumptions and the boundary conditions as well as the FEM discretisation and the solution. Various numerical results are subsequently presented which reflect the influence of both the temperature and the pore pressure on the development of the thermal instabilities at the heated surface of the concrete element. Finally, the simulated behaviour is compared with observations made during full-scale fire testing of concrete slabs. It is argued that thermal buckling of a delaminating heated surface layer due to increasing thermal stresses leads to the spalling mechanism (Lottman, 2017).

2 Schematisation of a fire exposed concrete structural element

A 2D cross-section, representing part of a concrete structural element, is schematised as shown in figure 2. Both the physical and fracture mechanics behaviour are described by separate FEM-based models, implemented for a heterogeneous material description. The aggregate particles, surrounding mortar and interfacial zones are each characterised by temperature-dependent material properties with especially the influence of the chemical dehydration of the cement paste considered (Alonso & Fernandez, 2004). The element is exposed to a single sided fire which is assumed constant in height direction. This later dimension is chosen several times larger than the width in order to obtain a representative cross-section. In depth direction the element has a unit thickness which assumes the concrete components as constant in order to consider only in-plane behaviour.

Along the top and bottom edges boundary conditions are imposed in order to mitigate the possible development of edge effects. With respect to the temperature and pore pressure development continuous boundaries are assumed. A predominately 1D behaviour, perpendicular to the heated surface, is obtained. Structural support conditions govern the deformations and resulting stresses, assuming that the thickness in depth direction is sufficient to restrain the deformations.

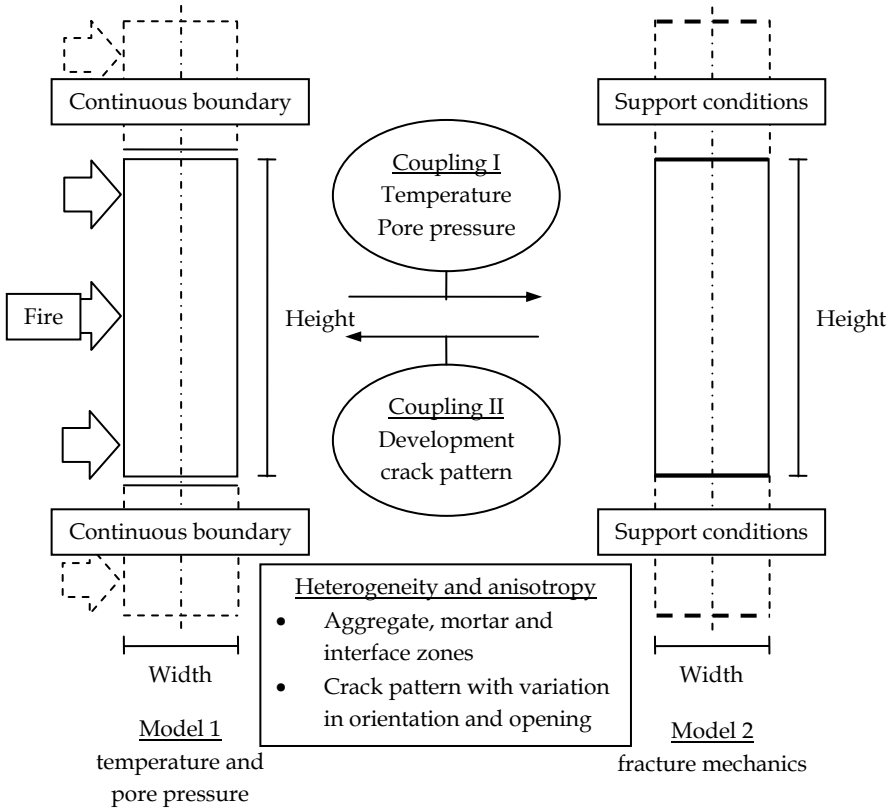

Figure 2: Schematic overview of the FEM model based on a representative part of a concrete structural element indicating materials, boundary conditions and couplings (Lottman, 2017)

Model 1 - temperature and pore pressure

The first FEM model focuses on the physical behaviour in which fire exposure causes the propagation of heat or thermal energy into the cross-section (Kordina, 1963). A temperature gradient develops governed by the relatively low thermal conductivity of the concrete (Kordina, 1963). These increasing temperatures also cause the evaporation of liquid water, present in the porous microstructure, giving rise to vapour pressures (Harmathy, 1965). The resultant pore pressure gradient drives the flow of the water phases through the pore space characterised by the relatively low permeability of concrete (Harmathy, 1965). At especially the left outer edge drainage of the water phases to the heated surrounding environment occurs.

Model 2 - fracture mechanics

The mechanical behaviour is governed by the second FEM model which reflects both the structural restraint and external loading as well as the temperature and pore pressure coupling. The temperature gradient causes differences in thermal expansion in the cross-section and between the concrete components (Hartsuijker & Welleman, 2007; van Breugel, et al., 1998). Based on this type of internal loading a thermal stress state develops which is characterised by partial restraint of the heated surface layer and tensile loading of the unheated centre (van Breugel, et al., 1998). The pore pressures, commonly not considered as internal load, are included through localised stress contributions (Gray & Schrefler, 2001).

Development of the crack pattern

The presence and influence of cracks are explicitly included in both FEM models. Due to the temperature gradient elastic stresses arise in the cross-section which are sufficient to fracture the concrete. A crack pattern develops in the cross-section with the opening causing non-linear deformations and relaxation of stresses in the surrounding material. This crack pattern is through the second coupling also considered to influence the pore pressure development by locally increasing the permeability dependent on the crack opening. Both FEM models are under these circumstances characterised as anisotropic governed by the direction of the cracks.

3 Definition of the FEM-based temperature and pore pressure model

This material description is based on the conservation of thermal energy and mass of the water phases across a representative elementary volume (REV) (Bear, 1972 / 1988; Hassanizadeh & Gray, 1979b). The most common approach is to use an Eulerian description in which the REV is defined for a fixed spatial field (Bear, 1972 / 1988). This allows to focus on the conservation of an averaged density, considering the influence by fluxes and sources (Hassanizadeh & Gray, 1979a; Bachmat & Bear, 1986). For each averaged densities a partial differential equation (PDE) is stated, governed by various non-linear material characterisations, while coupling is based on the process of evaporation (Tenchev, et al., 2001; Gawin, et al., 2003).

Conservation of thermal energy

The conservation of thermal energy is governed by the density and the specific heat capacity of the material with the temperature as variable (Bear, 1972 / 1988). Addition of the isotropic heat flux, characterised by Fourier's law of thermal conductivity (Bear, 1972 / 1988), and considering the consumption of energy by evaporation states the resultant PDE:

$$\rho C \frac{\partial T}{\partial t} + \boldsymbol{\nabla} \cdot \boldsymbol{q_T} = -H_{vap} \frac{\partial \overline{\rho_{vap}}}{\partial t} \tag{1}$$

with

$\boldsymbol{q_T} = -\boldsymbol{k}\boldsymbol{\nabla}T$

Conservation of the water phases

The gas phase is assumed to only consist of an ideal vapour with the contribution by dry air neglected based on the absence of a corresponding source. The partial vapour pressure is defined by the Relative Humidity (RH), based on the capillary pressure and Kelvin's equation, as well as the saturation pressure (Bear, 1972 / 1988; Pel & Huinink, 2007). Darcy's law, governed by the permeability of the material, characterises the vapour mass flux and is initially assumed isotropic (Bear, 1972 / 1988). The obtained PDE also reflects the addition of mass by the process of evaporation:

$$\frac{\partial \left(n(1-S_w)\frac{RHP_{sat}M_w}{RT}\right)}{\partial T}\frac{\partial T}{\partial t} + \frac{\partial \left(n(1-S_w)\frac{RHP_{sat}M_w}{RT}\right)}{\partial P_c}\frac{\partial P_c}{\partial t} + \boldsymbol{\nabla} \cdot \boldsymbol{q_{gw}} = \frac{\partial \overline{\rho_{vap}}}{\partial t} \tag{2}$$

with

$$\boldsymbol{q_{gw}} = -n(1-S_w)\frac{RHP_{sat}M_w}{RT}\left(\frac{K_{rel_g}}{\mu_g}\right)\boldsymbol{K}\boldsymbol{\nabla}P_{gw}$$

$$\boldsymbol{\nabla}P_{gw} = \boldsymbol{\nabla}(RHP_{sat}) = \frac{\partial(RHP_{sat})}{\partial T}\boldsymbol{\nabla}T + \frac{\partial(RHP_{sat})}{\partial P_c}\boldsymbol{\nabla}P_c$$

The mass conservation of the liquid water phase takes a similar form with the saturation level defined by the desorption isotherm according to (Genuchten, 1980). The water pressure is governed by the pressure difference across the concave meniscus as expressed by the capillary pressure, assuming both phases are immiscible (Bear, 1972 / 1988; Pel & Huinink, 2007). Inserting the liquid water flux and considering the subtraction of mass by evaporation obtains this PDE:

$$\frac{\partial(nS_w\rho_w)}{\partial T}\frac{\partial T}{\partial t} + \frac{\partial(nS_w\rho_w)}{\partial P_c}\frac{\partial P_c}{\partial t} + \boldsymbol{\nabla} \cdot \boldsymbol{q_w} = -\frac{\partial \overline{\rho_{vap}}}{\partial t} \tag{3}$$

with

$$\boldsymbol{q_w} = -nS_w\rho_w\left(\frac{K_{rel_w}}{\mu_w}\right)\boldsymbol{K}\boldsymbol{\nabla}P_w$$

$$\boldsymbol{\nabla}P_w = \boldsymbol{\nabla}\left(P_{gw} - P_c\right) = \frac{\partial(RHP_{sat})}{\partial T}\boldsymbol{\nabla}T + \left(\frac{\partial(RHP_{sat})}{\partial P_c} - 1\right)\boldsymbol{\nabla}P_c$$

Coupled system of PDE's

The influence of the evaporation process is obtained by assuming an instantaneous development according to the thermodynamic equilibrium defined by the desorption isotherm (Tenchev, et al., 2001; Gawin, et al., 2003). After rearranging and introducing mass and stiffness coefficients reflecting the time derivatives as well as the heat and mass fluxes respectively, the unsymmetrical coupled system of PDE's is obtained (Lottman, et al., 2011; Lottman, et al., 2013). The non-linearity in the material schematisation is based on the forced drying, affecting both the stiffness and especially the mass of the system:

$$\begin{gathered}\left(\begin{bmatrix} C_{TT_1} & 0 \\ C_{PT} & C_{PP}\end{bmatrix} + H_{vap}\begin{bmatrix} C_{TT_2} & C_{TP} \\ 0 & 0\end{bmatrix}\right)\begin{bmatrix}\dfrac{\partial T}{\partial t} \\ \dfrac{\partial P_c}{\partial t}\end{bmatrix} \\ -\boldsymbol{\nabla}\cdot\left(\begin{bmatrix} K_{TT_1} & 0 \\ K_{PT} & K_{PP}\end{bmatrix}\begin{bmatrix}\boldsymbol{\nabla}T \\ \boldsymbol{\nabla}P_c\end{bmatrix}\right) - H_{vap}\boldsymbol{\nabla}\cdot\left(\begin{bmatrix} K_{TT_2} & K_{TP} \\ 0 & 0\end{bmatrix}\begin{bmatrix}\boldsymbol{\nabla}T \\ \boldsymbol{\nabla}P_c\end{bmatrix}\right) = 0\end{gathered} \tag{4}$$

with

$$C_{TT_1} = \rho C \qquad C_{TT_2} = \frac{\partial\left(n(1-S_w)\dfrac{RHP_{sat}M_w}{RT}\right)}{\partial T}$$

$$C_{TP} = \frac{\partial\left(n(1-S_w)\dfrac{RHP_{sat}M_w}{RT}\right)}{\partial P_c}$$

$$C_{PT} = \frac{\partial(nS_w\rho_w)}{\partial T} + \frac{\partial\left(n(1-S_w)\dfrac{RHP_{sat}M_w}{RT}\right)}{\partial T}$$

$$C_{PP} = \frac{\partial(nS_w\rho_w)}{\partial P_c} + \frac{\partial\left(n(1-S_w)\dfrac{RHP_{sat}M_w}{RT}\right)}{\partial P_c}$$

$$K_{TT_1} = \boldsymbol{k} \qquad K_{TT_2} = n(1-S_w)\frac{RHP_{sat}M_w}{RT}\left(\frac{K_{rel_g}}{\mu_g}\right)\boldsymbol{K}\frac{\partial(RHP_{sat})}{\partial T}$$

$$K_{TP} = n(1-S_w)\frac{RHP_{sat}M_w}{RT}\left(\frac{K_{rel_g}}{\mu_g}\right)\boldsymbol{K}\frac{\partial(RHP_{sat})}{\partial P_c}$$

$$K_{PT} = nS_w\rho_w\left(\frac{K_{rel_w}}{\mu_w}\right)\boldsymbol{K}\frac{\partial(RHP_{sat})}{\partial T} + n(1-S_w)\frac{RHP_{sat}M_w}{RT}\left(\frac{K_{rel_g}}{\mu_g}\right)\boldsymbol{K}\frac{\partial(RHP_{sat})}{\partial T}$$

$$K_{PP} = nS_w\rho_w\left(\frac{K_{rel_w}}{\mu_w}\right)\boldsymbol{K}\left(\frac{\partial(RHP_{sat})}{\partial P_c} - 1\right) + n(1-S_w)\frac{RHP_{sat}M_w}{RT}\left(\frac{K_{rel_g}}{\mu_g}\right)\boldsymbol{K}\frac{\partial(RHP_{sat})}{\partial P_c}$$

Boundary conditions

This coupled system of PDE's is extended by Neumann boundary conditions reflecting the conservation of thermal energy and mass of the water phases along the left and right outer edges (van Kan, et al., 2008). Both temperature and capillary pressure are obtained through interaction with the ambient conditions, characterised at distance. Prescribed variables or Dirichlet boundary conditions (van Kan, et al., 2008) are in this case less desirable especially for the characterisation of the forced drying process which is a priori not known.

Interaction with the surrounding environment

The thermal energy is conserved by equilibration of both heat flux contributions and the external convective heat transfer based on the time-dependent development of the temperature (Tenchev, et al., 2001; Gawin, et al., 2003):

$$\begin{aligned} \left(\boldsymbol{q_T} + H_{vap}\boldsymbol{q_{gw}}\right)\cdot\boldsymbol{n}\big|_{\Gamma_A} &= \alpha_A(T - T_\infty) \\ -\left(K_{TT_1}\frac{\partial T}{\partial n} + H_{vap}\left(K_{TT_2}\frac{\partial T}{\partial n} + K_{TP}\frac{\partial P_c}{\partial n}\right)\right)\Big|_{\Gamma_A} &= \alpha_A(T - T_\infty) \end{aligned} \tag{5}$$

Similar considerations define the conservation of mass of the water phases which is governed by the external mass transfer through convection expressed in the water vapour density (Tenchev, et al., 2001; Gawin, et al., 2003):

$$\begin{aligned} \left(\boldsymbol{q_w} + \boldsymbol{q_{gw}}\right)\cdot\boldsymbol{n}\big|_{\Gamma_A} &= \beta_A\left(\rho_{gw} - \rho_{gw_\infty}\right) \\ -\left(K_{PT}\frac{\partial T}{\partial n} + K_{PP}\frac{\partial P_c}{\partial n}\right)\Big|_{\Gamma_A} &= \beta_A\left(\rho_{gw} - \rho_{gw_\infty}\right) \end{aligned} \tag{6}$$

Imposing continuity in height direction

Along the top and bottom edges periodical boundary conditions are implemented to mitigate the development of edge effects (Segal, 2008). This affectively implies that the top edge is connected to the bottom edge and both the heat and the mass fluxes are able to pass into adjacent cross-sections and vice versa. This causes both fluxes to be orientated predominantly perpendicular to the heated surface with at the moment not considering the influence of heterogeneity in the form of aggregate particles and local crack formation.

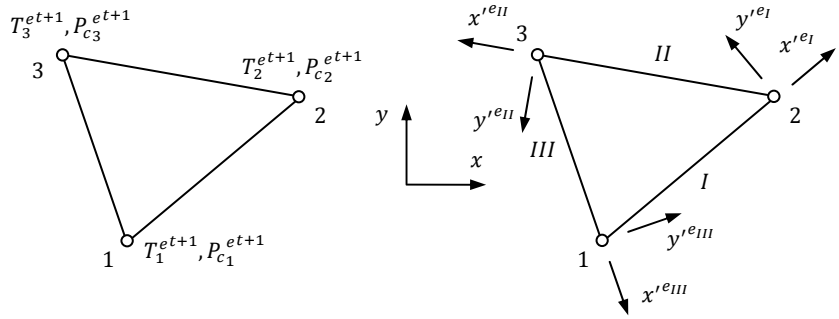

Figure 3: Linear approximation of the variables across a 2D triangular element in $\mathbb{R}^2$ (left). Schematic overview of the local coordinate systems used to define the anisotropic mass fluxes governing the water phases (right) (Lottman, 2017)

FEM discretisation

The FEM-based model is obtained by first restating the coupled system of PDE's or strong form in its weak form through minimisation of energy while also considering the Neumann boundary conditions (van Kan, et al., 2008; Zienkiewicz, et al., 2005). Thereafter Galerkin's method is used to obtain the finite element discretisation, consisting of both element mass and stiffness matrices (van Kan, et al., 2008; Zienkiewicz, et al., 2005). Time integration is based on an Euler backward scheme in order to enhance the numerical stability (van Kan, et al., 2008; Segal, 2008) whereas an incremental definition of the variables allows the use of a predictor to increase the speed of convergence. Spatial integration is implemented through a random discretisation by linear-based triangular elements as can be seen in figure 3 (van Kan, et al., 2008; Felippa, 2004a).

Implementation of heterogeneity

The main assumption for the heterogeneity is that the mortar and interfacial zones are schematised as porous material according to the coupled system of PDE's. The aggregate particles or solid material is assumed impermeable and only conducts thermal energy. This requires local reduction of the system of PDE's to only reflect the basic differential equation governed by Fourier's law. Affectively this introduces boundary conditions at the edges of the particles across which the mass fluxes of both water phases are not allowed. The distribution of the components is obtained by overlaying the discretised cross-section with a scanned image of an actual concrete mixture in order to determine the element properties (Schlangen, 1993; Vervuurt, 1997).

Implementation of anisotropy

At this point both the heat and mass fluxes are still assumed isotropic, neglecting possible directional dependence (Bear, 1972 / 1988). Cracks are included by introduction along each path of a local direction-dependent or anisotropic permeability (Bear, 1972 / 1988). The sudden volume increase upon crack opening is not included since this redistribution of mass and coinciding pressure reduction would affect severely the numerical stability (Lottman, 2017).

The permeability increase is defined perpendicular to the crack width and based on the simplified flow between parallel plates, obtaining the quadratic relationship as stated below (Bear, 1972 / 1988). For fracture mechanics coupling local coordinate systems are defined along the edges of each triangular element as seen in the right picture of figure 3. The orientation of the local mass fluxes are defined by the edge having the largest crack opening, considering only the in-plane components of the permeability tensor (Bear, 1972 / 1988). The global element permeability tensor is obtained by second order coordinate transformation, obtaining the following expression (Bear, 1972 / 1988; Zienkiewicz, et al., 2005):

$$\boldsymbol{K^e} = \boldsymbol{T_\alpha}^{e_d T} \boldsymbol{K'}^{e_d} \boldsymbol{T_\alpha}^{e_d} \tag{7}$$

with

$$K_{cr}{}'^{e_d} = \frac{w'^{e_d 2}}{12}$$

$$\boldsymbol{T_\alpha}^{e_d} = \begin{bmatrix} \cos\alpha^{e_d} & \sin\alpha^{e_d} \\ -\sin\alpha^{e_d} & \cos\alpha^{e_d} \end{bmatrix} \qquad \boldsymbol{K'}^{e_d} = \begin{bmatrix} K_{xx}{}'^{e_d} & 0 \\ 0 & K_{yy}{}'^{e_d} \end{bmatrix} = \begin{bmatrix} 0 & 0 \\ 0 & K_{cr}{}'^{e_d} \end{bmatrix}$$

Numerical stability

Cracks represent localised and substantial discontinuities which increase the level of non-linearity in the numerical system to be solved. In order to maintain a sufficient speed of convergence and especially avoid oscillations in the solution an adaptive time stepping scheme is introduced (Söderlind & Wang, 2006). Furthermore, a mitigation of the level of anisotropy as well as an in-time gradual implementation of the permeability increase are used in order to maintain numerical stability.

In the relationship between the pore pressure and the crack opening further advances in the theoretical background of the FEM-model could be made. For instance, a higher order definition of the mass fluxes could be considered to smoothen the response of the system.

Validation of the numerical implementation

The numerical approximation of the system of coupled PDE's is validated by comparing the FEM-based solution with results obtained by means of the Finite Difference Method (FDM). For simplicity are the conservation of thermal energy and mass of the water phases both separately assessed using basic cases. The temperature and capillary pressure development through the cross-section, based on the progress of thermal energy and drying at a constant temperature respectively, are found to be sufficiently accurate (Lottman, 2017).

4 Definition of the FEM-based fracture mechanics model

This material description is based on the balance of linear momentum across a mechanical continuum (Timoshenko & Goodier, 1970). The most common approach is to use a Lagrangian description in which the continuum is defined for a fixed material field (Spencer, 1980 / 2004). This allows to focus on the translational equilibrium conditions for the continuum with the possibility to also consider the influence of large deformations (Spencer, 1980 / 2004) as could develop to indicate the spalling mechanism. This continuum is also assumed infinitesimal with the internal moments by the first order displacement approximation neglected as is commonly adopted (Spencer, 1980 / 2004; Wells, 2006).

Translational equilibrium

The balance of forces across the continuum considers only static contributions from the Cauchy stress tensor which in order to ensure equilibrium is symmetrical (Timoshenko & Goodier, 1970; Spencer, 1980 / 2004). The material is characterised as linear elastic and isotropic with the deformations expressed by infinitesimal strains (Spencer, 1980 / 2004; Wells, 2006). These strains are commonly approximated by linear varying displacements, obtaining a local or piecewise constant stress (Felippa, 2004a; Zienkiewicz, et al., 2005). The PDE is further simplified by neglecting the influence of distributed body forces such as self-weight (Spencer, 1980 / 2004; Wells, 2006):

$$\boldsymbol{\nabla} \cdot \underline{\boldsymbol{\sigma}} + \overset{=0}{\vec{\boldsymbol{f}}} = \boldsymbol{\nabla} \cdot \left(\boldsymbol{C} : \underline{\boldsymbol{\varepsilon}} \right) = 0 \tag{8}$$

Plane strain approximation

This linear elastic stress-strain relationship is commonly restated using engineering notation which also introduces the shearing strain to define the angular distortion between adjacent planes (Prezemieniecki, 1968 / 1985; Wells, 2006). A further simplification characterises the deformation in the out-of-plane direction which in case of the structural element is chosen to be restraint, obtaining the plane strain approximation (Timoshenko & Goodier, 1970; Prezemieniecki, 1968 / 1985). The temperature-induced expansion of the material is reflected as an imposed strain without shear contribution (Timoshenko & Goodier, 1970; Prezemieniecki, 1968 / 1985). As additional internal loading the pore pressure is considered based on an effective stress approach (Gray & Schrefler, 2001; Zienkiewicz, et al., 2005) or alternatively the stress state surrounding a pressure loaded pore (Timoshenko & Goodier, 1970). The PDE governing the mechanical continuum is thus restated, introducing also the gradient matrix of spatial derivatives (Prezemieniecki, 1968 / 1985; Zienkiewicz, et al., 2005):

$$\boldsymbol{B_U}^{\boldsymbol{T}}\boldsymbol{\sigma} = \boldsymbol{B_U}^{\boldsymbol{T}}(\boldsymbol{D}(\boldsymbol{\varepsilon} - \boldsymbol{\varepsilon_T}) + \boldsymbol{\sigma_P}) = 0 \tag{9}$$

with

$$\boldsymbol{\sigma} = \begin{bmatrix}\sigma_{xx}\\ \sigma_{yy}\\ \sigma_{xy}\end{bmatrix} \qquad \boldsymbol{\sigma_P} = \begin{bmatrix}\sigma_P\\ \sigma_P\\ 0\end{bmatrix}$$

$$\boldsymbol{\varepsilon} = \begin{bmatrix}\varepsilon_{xx}\\ \varepsilon_{yy}\\ \gamma_{xy}\end{bmatrix} = \begin{bmatrix}\varepsilon_{xx}\\ \varepsilon_{yy}\\ 2\varepsilon_{xy}\end{bmatrix} \qquad \boldsymbol{\varepsilon_T} = (1+\nu)\begin{bmatrix}\varepsilon_T\\ \varepsilon_T\\ 0\end{bmatrix}$$

$$\boldsymbol{D} = \frac{E}{(1+\nu)(1-2\nu)}\begin{bmatrix}1-\nu & \nu & 0\\ \nu & 1-\nu & 0\\ 0 & 0 & \dfrac{1-2\nu}{2}\end{bmatrix} \qquad \boldsymbol{B_U} = \begin{bmatrix}\dfrac{\partial}{\partial x} & 0\\ 0 & \dfrac{\partial}{\partial y}\\ \dfrac{\partial}{\partial y} & \dfrac{\partial}{\partial x}\end{bmatrix}$$

Boundary conditions

The PDE or in this case the equivalent engineering problem is extended by boundary conditions that characterise the deformation based on Bernoulli's hypothesis of plane cross-sections (Hartsuijker & Welleman, 2007). This is the most common assumption used for beams and states that during deformation each cross-section remains perpendicular to the longitudinal axis, neglecting the possibility for additional rotation by shear deformation. For the structural element considered this involves the upper and low boundary edges individually as seen in figure 4 for which the deformation is described by both axial translation and rotation.

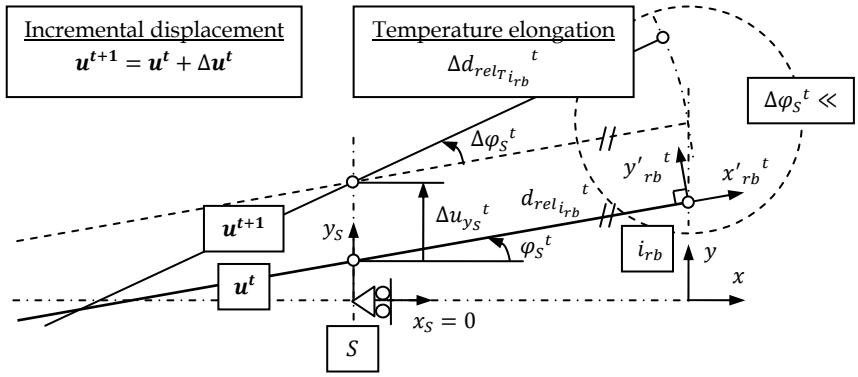

Figure 4: The rigid body motion of each cross-sectional outer edge is characterised by axial translation and rotation relative to the central support as shown in $\mathbb{R}^2$ (Lottman, 2017)

Central supports with fixed horizontal direction

This linear strain definition is imposed along the top and bottom outer edges as rigid body motions relative to central supports (Hartmann & Katz, 2007). Each central support is governed by a combination of Dirichlet and Neumann boundary conditions (van Kan, et al., 2008) with the former prescribing the support in the horizontal direction as fixed:

$$u_x|_{\Gamma_{S_D}} = 0 \tag{10}$$

The vertical or axial displacement and rotation are governed by the latter condition and are described hereafter by coupling conditions. Structural interaction is considered by assumed constant partial restraint with external loading imposed before fire exposure (Bouma, 2000):

$$\underline{\boldsymbol{\sigma}}\mathbf{n}\big|_{\Gamma_{S_N}} = -\mathbf{K_S u} + \mathbf{F_S} \tag{11}$$

with

$$\mathbf{F_S} = \begin{bmatrix} F_{y_S} \\ F_{\varphi_S} \end{bmatrix} \qquad \mathbf{K_S} = \begin{bmatrix} K_{y_S} & 0 \\ 0 & K_{\varphi_S} \end{bmatrix}$$

Coupling conditions to reflect displacements along the outer edge

The rigid bodies are formed through stating coupling conditions which define the deformational relationship along each of the outer edges (Hartmann & Katz, 2007). These geometric non-linear conditions are defined in incremental form along the deformed edge, using the assumption of small displacements and rotations as schematically shown in figure 4.

Each set of nodal displacements is expressed in the displacements at the support using the relative distance to the support as well as the rotation of the edge. This leads to a second order transformation tensor while also considering the global coordinates in the following definition as well as the incremental thermal elongation of the edge:

$$\Delta \boldsymbol{u}_{\boldsymbol{i_{rb}}}{}^{\boldsymbol{t}} = \boldsymbol{T}_{\boldsymbol{rb}_{\boldsymbol{i_{rb}}}}{}^{\boldsymbol{t}} \Delta \boldsymbol{u}_{\boldsymbol{S}}{}^{\boldsymbol{t}} + \Delta \boldsymbol{u}_{\boldsymbol{T}_{\boldsymbol{i_{rb}}}}{}^{\boldsymbol{t}} \tag{12}$$

with

$$\Delta \boldsymbol{u}_{\boldsymbol{i_{rb}}}{}^{\boldsymbol{t}} = \begin{bmatrix} \Delta u_{x_{i_{rb}}}{}^{t} \\ \Delta u_{y_{i_{rb}}}{}^{t} \end{bmatrix} \qquad \Delta \boldsymbol{u}_{\boldsymbol{S}}{}^{\boldsymbol{t}} = \begin{bmatrix} \Delta u_{y_S}{}^{t} \\ \Delta \varphi_S{}^{t} \end{bmatrix} \qquad \Delta \boldsymbol{u}_{\boldsymbol{T}_{\boldsymbol{i_{rb}}}}{}^{\boldsymbol{t}} = \begin{bmatrix} \cos\varphi_S{}^{t} \Delta d_{rel\,T_{i_{rb}}}{}^{t} \\ \sin\varphi_S{}^{t} \Delta d_{rel\,T_{i_{rb}}}{}^{t} \end{bmatrix}$$

$$\boldsymbol{T}_{\boldsymbol{rb}_{\boldsymbol{i_{rb}}}}{}^{\boldsymbol{t}} = \begin{bmatrix} 0 & -\sin\varphi_S{}^{t} d_{rel\,i_{rb}}{}^{t} \\ 1 & \cos\varphi_S{}^{t} d_{rel\,i_{rb}}{}^{t} \end{bmatrix}$$

FEM discretisation

The PDE or engineering problem stated above could be solved following the approach outlined for the FEM temperature and pore pressure model. In this case the resultant discretisation would use similar randomly orientated linear triangular elements (Felippa, 2004a; Zienkiewicz, et al., 2005). However, the adopted fracture mechanics approach uses a different basis. Three local extensional strains are defined in order to approximate the global strains, using the triangular element as basis (Prezemieniecki, 1968 / 1985; Blaauwendraad, 2004; Felippa, 2004a) as shown in figure 5. The following fourth order element-based transformation tensor relates these strains (Timoshenko & Goodier, 1970; Felippa, 2004a):

$$\boldsymbol{\varepsilon}'^{\boldsymbol{e}} = \boldsymbol{T}_{\boldsymbol{\varepsilon_M}}{}'^{\boldsymbol{e}} \boldsymbol{\varepsilon}^{\boldsymbol{e}} \tag{13}$$

with

$$\boldsymbol{T}_{\boldsymbol{\varepsilon_M}}{}'^{\boldsymbol{e}} = \begin{bmatrix} \cos^2\alpha^{e_I} & \sin^2\alpha^{e_I} & \sin\alpha^{e_I}\cos\alpha^{e_I} \\ \cos^2\alpha^{e_{II}} & \sin^2\alpha^{e_{II}} & \sin\alpha^{e_{II}}\cos\alpha^{e_{II}} \\ \cos^2\alpha^{e_{III}} & \sin^2\alpha^{e_{III}} & \sin\alpha^{e_{III}}\cos\alpha^{e_{III}} \end{bmatrix}$$

Material schematisation in the local directions

The approximated solution to the engineering problem consists of three contributions with the first characterised by the local material definition using a triangular orientation of 1D bars, assuming again plane strain (Prezemieniecki, 1968 / 1985; Blaauwendraad, 2004). Each bar is described by Hooke's law, relating the extensional strain and the axial stress while also considering the temperature-induced expansion and the effective stress resulting from the pore pressure (Timoshenko & Goodier, 1970).

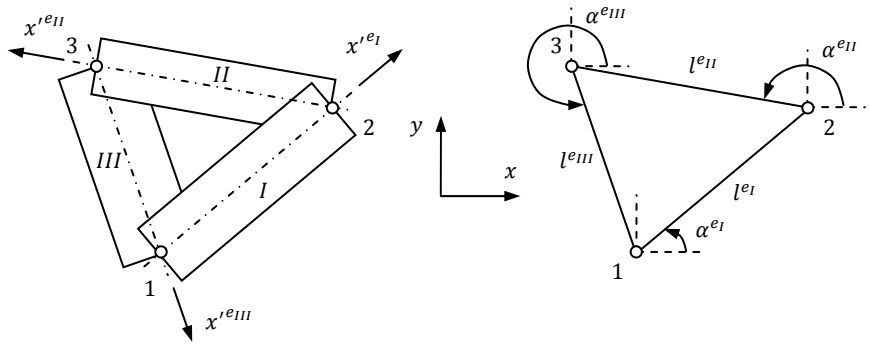

Figure 5: Schematic representation of three triangular orientated 1D bars in $\mathbb{R}^2$ (left). These characterise the local extensional strains along each of the element edges (right) (Lottman, 2017)

Second order coordinate transformation is used to obtain the global definition (Wells, 2006; Blom, 2009). Both the diagonal elasticity tensor and gradient matrix reflect the uncoupled axial directions, loaded by imposed temperature strains and pressure-induced stresses:

$$\boldsymbol{B_{U_M}}'^{\boldsymbol{eT}}\boldsymbol{\sigma}'^{\boldsymbol{e}} = \boldsymbol{B_{U_M}}'^{\boldsymbol{eT}}\left(\boldsymbol{D}'^{\boldsymbol{e}}\left(\boldsymbol{\varepsilon}'^{\boldsymbol{e}} - \boldsymbol{\varepsilon_T}'^{\boldsymbol{e}}\right) + \boldsymbol{\sigma_P}'^{\boldsymbol{e}}\right) = 0 \tag{14}$$

with

$$\boldsymbol{\sigma}'^{\boldsymbol{e}} = \begin{bmatrix} \sigma'^{e_I} \\ \sigma'^{e_{II}} \\ \sigma'^{e_{III}} \end{bmatrix} \qquad \boldsymbol{\sigma_P}'^{\boldsymbol{e}} = \begin{bmatrix} {\sigma_P}'^{e_I} \\ {\sigma_P}'^{e_{II}} \\ {\sigma_P}'^{e_{III}} \end{bmatrix}$$

$$\boldsymbol{\varepsilon}'^{\boldsymbol{e}} = \begin{bmatrix} \varepsilon'^{e_I} \\ \varepsilon'^{e_{II}} \\ \varepsilon'^{e_{III}} \end{bmatrix} \qquad \boldsymbol{\varepsilon_T}'^{\boldsymbol{e}} = (1+\nu)\begin{bmatrix} {\varepsilon_T}'^{e_I} \\ {\varepsilon_T}'^{e_{II}} \\ {\varepsilon_T}'^{e_{III}} \end{bmatrix}$$

$$\boldsymbol{D}'^{\boldsymbol{e}} = \frac{1}{1-\nu^2}\begin{bmatrix} E'^{e_I} & 0 & 0 \\ 0 & E'^{e_{II}} & 0 \\ 0 & 0 & E'^{e_{III}} \end{bmatrix} \qquad \boldsymbol{B_{U_M}}'^{\boldsymbol{e}} = \begin{bmatrix} \dfrac{\partial}{\partial x'^{e_I}} & 0 & 0 \\ 0 & \dfrac{\partial}{\partial x'^{e_{II}}} & 0 \\ 0 & 0 & \dfrac{\partial}{\partial x'^{e_{III}}} \end{bmatrix}$$

To consider the previously derived incremental rigid body motions and to anticipate the hereafter addressed large deformations is first the material-based stress increment defined, reflecting both time and crack dependence (Schlangen, 1993; Vervuurt, 1997). The first of the three terms considers the non-linear degradation of Young's modulus, requiring redistribution of stresses in order to preserve elastic strain energy. The latter terms reflect the temperature strain and pressure-induced stress development loading the material:

$$\Delta\boldsymbol{\sigma}'^{\boldsymbol{et+1}}_{\boldsymbol{k}} = \Delta\boldsymbol{D}'^{\boldsymbol{et+1}}_{\boldsymbol{k}}\left(\boldsymbol{\varepsilon}'^{\boldsymbol{et+1}}_{\boldsymbol{k}} - {\boldsymbol{\varepsilon_T}}'^{\boldsymbol{et+1}}_{\boldsymbol{k}}\right) + \boldsymbol{D}'^{\boldsymbol{et+1}}_{\boldsymbol{k}}\left(\Delta\boldsymbol{\varepsilon}'^{\boldsymbol{et+1}}_{\boldsymbol{k}} - \Delta{\boldsymbol{\varepsilon_T}}'^{\boldsymbol{et+1}}_{\boldsymbol{k}}\right) + \Delta{\boldsymbol{\sigma_P}}'^{\boldsymbol{et+1}}_{\boldsymbol{k}} \tag{15}$$

Geometrical dependent force transfer

The second contribution is geometrical-based and considers the influence of large deformations on the translation equilibrium conditions (Bathe, 1986; Gavin, 2014). For the bars this implies translation and rotation of the normal forces to align with the deformed state (Bathe, 1986; Gavin, 2014). An additional condition is stated by conservation of elastic strain energy while considering that during incremental deformations the loaded material is both stretched and rotated (Bathe, 1986; Gavin, 2014).

For each bar the incremental strain and rotation are defined using the small displacements assumption as expressed in the local coordinate system aligned with the current deformed state (Bathe, 1986; Gavin, 2014):

$$\Delta\varepsilon'^{e_d}{}_k^{t+1} = \frac{\Delta l^{e_d}{}_k^{t+1}}{l^{e_d}{}_k^{t+1}} = \frac{\Delta u_x{}'^{e_d}{}_{2\ k}^{t+1} - \Delta u_x{}'^{e_d}{}_{1\ k}^{t+1}}{l^{e_d}{}_k^{t+1}}$$
$$\Delta\alpha^{e_d}{}_k^{t+1} \approx \frac{\Delta u_y{}'^{e_d}{}_{2\ k}^{t+1} - \Delta u_y{}'^{e_d}{}_{1\ k}^{t+1}}{l^{e_d}{}_k^{t+1}} \tag{16}$$

Both incremental deformations can be used to decompose the normal force or alternatively the axial stress acting in the current deformed bar while considering that the cross-section is assumed to remain constant (Bathe, 1986; Gavin, 2014). Two terms are obtained with the former reflecting the current state and the latter based on the incremental deformations:

$$\begin{bmatrix} N_x{}'^{e_d} \\ N_y{}'^{e_d} \end{bmatrix}_k^{t+1} = \int_{A^{e_d}} \begin{bmatrix} \sigma'^{e_d}\cos\Delta\alpha^{e_d} \\ \sigma'^{e_d}\sin\Delta\alpha^{e_d} \end{bmatrix}_k^{t+1} dA^{e_d} \approx A^{e_d}\left(\begin{bmatrix} \sigma'^{e_d} \\ 0 \end{bmatrix}_k^{t+1} + \begin{bmatrix} \sigma'^{e_d}\Delta\varepsilon_m{}'^{e_d} \\ \sigma'^{e_d}\Delta\alpha^{e_d} \end{bmatrix}_k^{t+1}\right) \tag{17}$$

The second term stated above governs the additional incremental stress that develops in each bar based on the straining and rotation of the material (Bathe, 1986; Gavin, 2014). An additional relationship for the three bars can thus be derived through definition of a geometrical non-linear gradient matrix. The local horizontal and vertical incremental displacements again require second order coordinate transformation (Wells, 2006; Blom, 2009) to obtain the definition expressed in the global coordinate system:

$$\boldsymbol{B_{U_G}}'^{\boldsymbol{e}t+1}{}_{\boldsymbol{k}}^{\boldsymbol{T}} \begin{bmatrix} \boldsymbol{\sigma}'^{\boldsymbol{e}t+1}_{\boldsymbol{k}} & 0 \\ 0 & \boldsymbol{\sigma}'^{\boldsymbol{e}t+1}_{\boldsymbol{k}} \end{bmatrix} \begin{bmatrix} \Delta\boldsymbol{\varepsilon_m}'^{\boldsymbol{e_d}t+1}_{\boldsymbol{k}} \\ \Delta\boldsymbol{\alpha}^{\boldsymbol{e_d}t+1}_{\boldsymbol{k}} \end{bmatrix} = \boldsymbol{B_{U_G}}'^{\boldsymbol{e}t+1}{}_{\boldsymbol{k}}^{\boldsymbol{T}} \begin{bmatrix} \boldsymbol{\sigma}'^{\boldsymbol{e}t+1}_{\boldsymbol{k}} & 0 \\ 0 & \boldsymbol{\sigma}'^{\boldsymbol{e}t+1}_{\boldsymbol{k}} \end{bmatrix} \boldsymbol{B_{U_G}}'^{\boldsymbol{e}t+1}{}_{\boldsymbol{k}} \Delta\boldsymbol{u}'^{\boldsymbol{e}t+1}_{\boldsymbol{k}} = 0 \tag{18}$$

with

$$\begin{bmatrix} \Delta \boldsymbol{u_x}'^{\boldsymbol{e}t+1}_{\boldsymbol{k}} \\ \Delta \boldsymbol{u_y}'^{\boldsymbol{e}t+1}_{\boldsymbol{k}} \end{bmatrix} = \begin{bmatrix} \Delta {u_x}'^{e_I t+1}_{k} \\ \Delta {u_x}'^{e_{II} t+1}_{k} \\ \Delta {u_x}'^{e_{III} t+1}_{k} \\ \Delta {u_y}'^{e_I t+1}_{k} \\ \Delta {u_y}'^{e_{II} t+1}_{k} \\ \Delta {u_y}'^{e_{III} t+1}_{k} \end{bmatrix} \qquad \boldsymbol{B_{U_G}}'^{\boldsymbol{e}t+1}_{\boldsymbol{k}} = \begin{bmatrix} \frac{\partial}{\partial \boldsymbol{x}'^{\boldsymbol{e}t+1}_{\boldsymbol{k}}} & 0 \\ 0 & \frac{\partial}{\partial \boldsymbol{x}'^{\boldsymbol{e}t+1}_{\boldsymbol{k}}} \end{bmatrix}$$

$$\frac{\partial}{\partial \boldsymbol{x}'^{\boldsymbol{e}t+1}_{\boldsymbol{k}}} = \begin{bmatrix} \frac{\partial}{\partial {x'}^{e_I t+1}_{k}} & 0 & 0 \\ 0 & \frac{\partial}{\partial {x'}^{e_{II} t+1}_{k}} & 0 \\ 0 & 0 & \frac{\partial}{\partial {x'}^{e_{III} t+1}_{k}} \end{bmatrix}$$

Implementation of heterogeneity

Heterogeneity is governed by the same procedure as described for the FEM temperature and pore pressure model. However, each of the three bars is individually characterised by the concrete components, using the same mechanical schematisation. The resultant local elasticity tensor is through the previously stated fourth order transformation tensor expressed in the global stiffness as defined by (Felippa, 2004a; Zienkiewicz, et al., 2005):

$$\boldsymbol{D^e} = \boldsymbol{T_{\varepsilon_M}}'^{\boldsymbol{eT}} \boldsymbol{D'^e} \boldsymbol{T_{\varepsilon_M}}'^{\boldsymbol{e}} \tag{19}$$

Similar considerations also allow to transform the local axial stress vector in order to obtain the global stresses (Felippa, 2004a; Zienkiewicz, et al., 2005). This relationship proves convenient in order to determine the accuracy of the adopted triangular approximation by considering several basic load cases:

$$\boldsymbol{\sigma^e} = \boldsymbol{T_{\varepsilon_M}}'^{\boldsymbol{eT}} \boldsymbol{\sigma'^e} \tag{20}$$

Implementation of anisotropy

The level of anisotropy in these relationships is initially characterised by the variation of Young's modulus and is extended in case cracks are considered. The adopted fracture mechanics approach assumes that the stiffness across the crack is negligible (Schlangen, 1993; Vervuurt, 1997). This is implemented by removal of bars, through the local elasticity tensor, based on brittle fracture by the stress exceeding the tensile strength (Schlangen, 1993; Vervuurt, 1997). Redistribution of the fracture forces conserves the elastic strain energy and governs the crack propagation as is shown in figure 6.

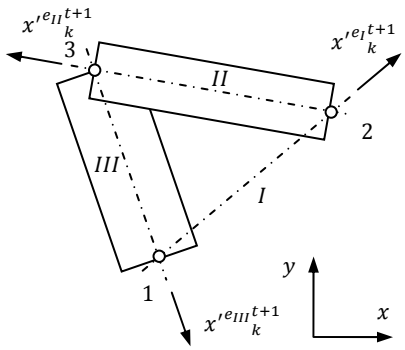

Modified local elasticity tensor

$$\boldsymbol{D'}^{\boldsymbol{e}\boldsymbol{t+1}}_{\boldsymbol{k+1}} = \frac{1}{1-\nu^2}\begin{bmatrix} 0 & 0 & 0 \\ 0 & E'^{e_{II}}{}_{k+1}^{t+1} & 0 \\ 0 & 0 & E'^{e_{III}}{}_{k+1}^{t+1} \end{bmatrix}$$

Modified local stress vector

$$\boldsymbol{\sigma'}^{\boldsymbol{e}\boldsymbol{t+1}}_{\boldsymbol{k+1}} = \begin{bmatrix} 0 \\ \sigma'^{e_{II}}{}_{k+1}^{t+1} \\ \sigma'^{e_{III}}{}_{k+1}^{t+1} \end{bmatrix}$$

Figure 6: Schematic representation of a cracked set of three triangular orientated 1D bars in $\mathbb{R}^2$*. After fracture both the local elasticity tensor and stress vector are modified to represent the assumed stress-free crack edge* (Lottman, 2017)

Numerical stability

The third and final contribution to the mechanical system leads to the traditional lattice approach as used by (Schlangen, 1993; Vervuurt, 1997) considering in this application also geometrical non-linearity. Due to the removal of the bars and thus the directional stiffness, discontinuities are introduced in the material. This could cause too localised deformations and insufficient redistribution of fracture forces to the surrounding material since the three axial strains are together required to approximate the global strains. In the lattice approach Bernoulli-Euler beams are added to characterise the nodal rotations by addition of stiffness thus stabilising the mechanical response (Schlangen, 1993; Vervuurt, 1997).

Further advances regarding the fundamental background of the lattice should be made. The inherent assumption in a basic continuum of not considering rotational equilibrium of forces could form the starting point in modifying the definition of the anisotropic bars.

Validation of the numerical implementation

The local schematisation of the global strains by three extensional strains is validated by comparison of the FEM-based solution with results obtained by stating basic equilibrium of forces. For this purpose the element definition is restated slightly to reflect a plane stress approximation of the continuum. Validation of the plane strain continuum relies on direct comparison of FEM results using triangular elements. For both sufficiently accurate results are obtained using various basic load cases such as external forces and moments as well as constant, linear and gradients in temperature (Lottman, 2017).

5 FEM discretisation of the structural element

The FEM model presented is used to assess the influence of severe fire exposure on a cross-section having varying concrete strength classes and aggregate types. The height and width, shown in figure 7, are 600 mm and 250 mm respectively. The edges of the randomly orientated triangular element discretisation are on average 2,5 mm. This relatively small internal length scale allows for sufficient detail in the crack pattern while still limiting the number of degrees of freedom at the nodes.

The largest aggregates in this cross-section have a width of around 25 mm with also some smaller sizes filling the space in between. Symmetry of the material with respect to the horizontal central axis ensures correct implementation of the periodical boundary conditions. For additional information regarding the FEM schematisation such as the element discretisation and implementation as well as the boundary conditions and the material properties the reader is referred to (Lottman, 2017).

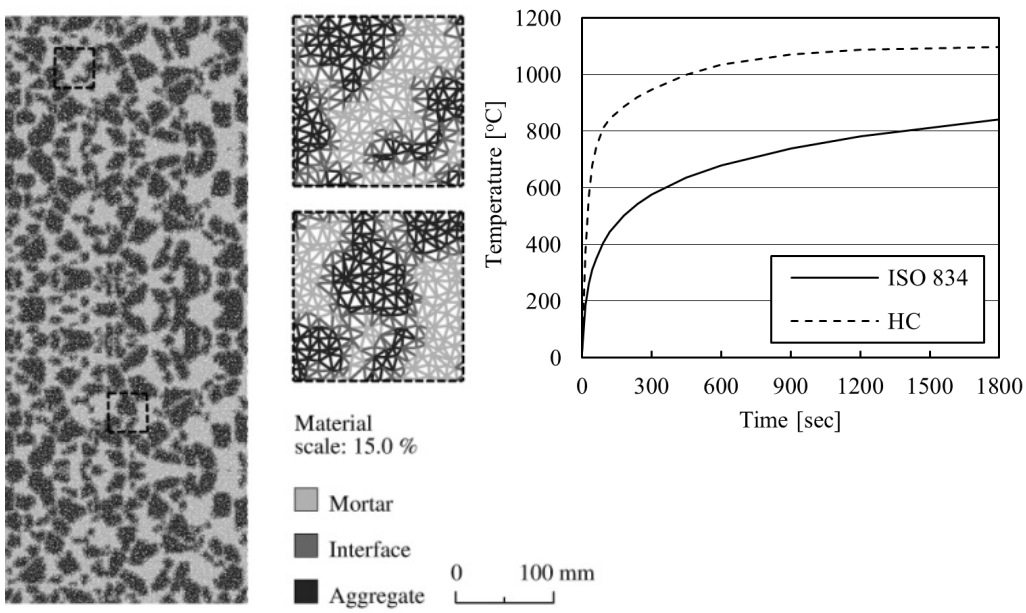

Figure 7: Discretisation of the cross-section by triangularly orientated 1D elements to numerically approximate the heterogeneous and anisotropic behaviour (Lottman, 2017). *The fire scenarios are based on exposure to a standard fire (ISO 834) or a hydro carbon fire (HC)* (Eurocode 1, 2011a)

6 Crack development due to the temperature gradient

The fracture behaviour is first investigated by assuming that only temperature development occurs. For this purpose the FEM model is simplified to only reflect thermal conductivity based on the concrete components. The cross-section is exposed to a fire corresponding to a hydrocarbon scenario which rapidly develops in the first 2 minutes and reaches a temperature of more than 1000 ^{o}C after 600 seconds as reflected by the right graph in figure 7 (Eurocode 1, 2011a). This scenario represents a similar high fire loading as the RWS fire curve, stated in the guidelines by Rijkswaterstaat (RWS, 2017) and commonly used in the Netherlands as well as abroad.

Deformation and crack development of a NSC cross-section

The consequences of this type of severe fire exposure first depends on the chosen aggregate type, governing the thermal expansion through the imposed internal loading (Eurocode 2, 2011b). The Normal Strength Concrete (NSC) cross-section with a strength class of C25/30 shown in the left picture of figure 8 is under these circumstances still assumed to be unrestraint which allows several large cracks to develop. Compared to the surrounding weaker mortar and especially the interfacial zones the particles cause extensive cracking in the heated surface zone (Lottman, et al., 2011). The level of cracking, starting at on the onset of fire exposure, is sufficient to relax most of the stresses and seriously damage the cross-section.

Addition of partial restraint is the second aspect that is considered. The crack pattern again directly develops at the start of fire exposure. However, compared to the unrestrained conditions the stress state and the crack pattern change as is indicated by the right picture of figure 8. Vertical cracks parallel to the heated surface develop with the structural restraint ensuring that the compressive stresses remain present. In the centre of the cross-section horizontal cracks are estimated to develop, relaxing the overall stress state while exhibiting a reduction in the level of opening.

Formation of unstable heated surface layers

The main difference between both simulations is that the latter indicates the formation of thermal instabilities at the heated surface. After around 300 seconds of fire exposure several large cracks in the transition zone with the unheated centre of the cross-section develop. Also several inclined cracks are present, reflecting the steep gradient in the

thermal stresses (Lottman, et al., 2011). In the time interval to 600 seconds the maximum compressive stress increase from 20 MPa to 30 MPa (Lottman, 2017). Especially at the start of these deformations this is lower than the temperature-dependent compressive strength of C25/30 (RILEM TC-HTC, 2004). The continued fire exposure extends the crack pattern and a curved fracture surface develops along the rear of the heated surface layer.

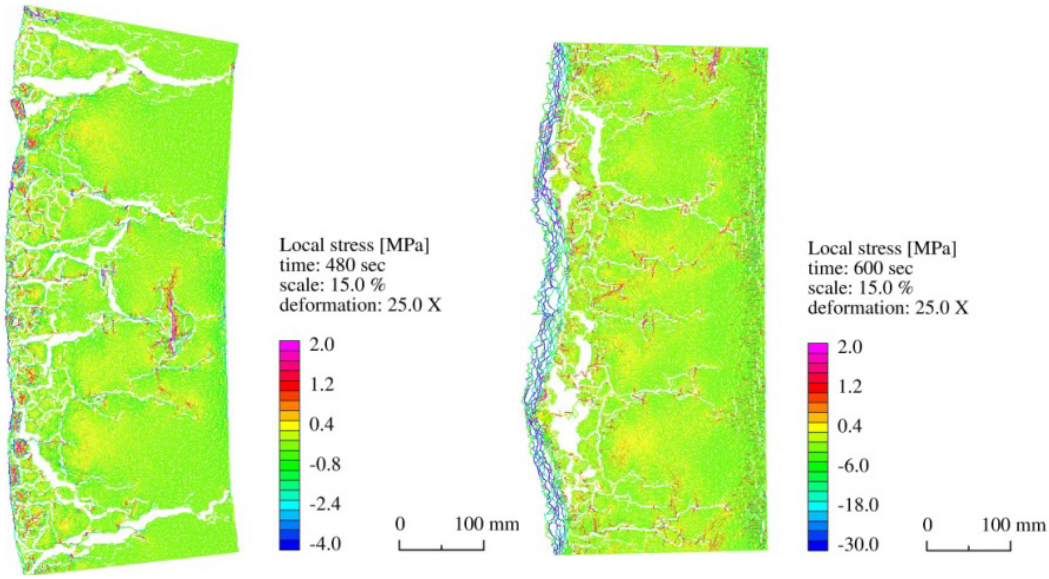

Figure 8: Addition of partial restraint for a C25/30 cross-section exposed to a severe fire changes the structural behaviour from several large cracks across the width while relaxing most of the stresses (left) to surface-based instabilities under sustained compressive loading (right) (Lottman, 2017)

The formation and deformation of seemingly unstable pieces of concrete at the heated concrete surface could be argued as one of the first numerical computations of a spalling mechanism. Moreover, various other simulations analysed in (Lottman, 2017) revealed the same tendency for other material and loading scenarios. This could suggest that these relatively slender compressed heated surface layers are part of a developing thermal buckling process (Lottman, 2017).

Observations of the crack patterns arising from the temperature gradient

Fire exposure and especially hydrocarbon-based scenarios represent a severe type of thermal loading for the concrete cross-section. The distinctive load case that develops is characterised by a steep gradient in the thermal stresses, starting from the onset of fire exposure and causing cracks in the tensile loaded centre of the cross-section. In case

structural restraint is present, the compressive restraining force acting in the heated surface layer is also preserved. The consequences of these stresses can for instance be observed by the cracks that develop at the concrete surface of fire exposed slabs (FSV, 2004; Horvath, et al., 2004). Moreover, the possibility for a dehydrated and cracked slab to fail in unrestrained conditions also seems likely to occur as for instance reported by (Horvath, et al., 2004). Observing the consequences of the thermal restraining is more difficult based on the limited thickness of the heated surface layer and the relative small cracks.

7 Pore pressure reduction based on crack development

The possibility for unstable layers to develop at the heated concrete surface is only based on the temperature gradient acting as internal loading. The question remains if the pore pressure can contribute as is investigated for the previously discussed partially restrained cross-section. For this purpose are both the solid and porous material characterisation used in the FEM temperature and pore pressure model. With respect to this simulation it needs to be considered that including forced drying using the fracture mechanics coupling requires the largest calculation times due to a lower rate of convergence and a smaller size of the time step.

Drying of a cracked NSC cross-section during severe fire exposure

The forced drying process is driven by the imposed severity of the type of fire exposure and the conditioning of the cross-section to an external climate with a RH of 80 % (Khoury, 2008a). Without considering the cracks the gas pressure can, in these circumstances, exceed 1,5 MPa (Lottman, 2017) which is higher than the tensile strength of NSC (RILEM TC-HTC, 2004). Local pressure peaks can also arise by the presence of especially the larger aggregate particles, impeding the flow towards the heated surface.

However, this simulation reveals that the extensive crack development in the heated surface layer largely reduces the pressures (Lottman, et al., 2015) as seen in the left picture of figure 9. Moreover, the pore pressure no longer represents a continuous front, but varies depending on the vicinity of cracks and the permeability of the surrounding material. With respect to these cross-sectional results it is recalled that the first FEM model uses a numerically approximation based on triangular elements. Cracks are considered in the material properties and through this approach influence the distribution of the gas pressures.

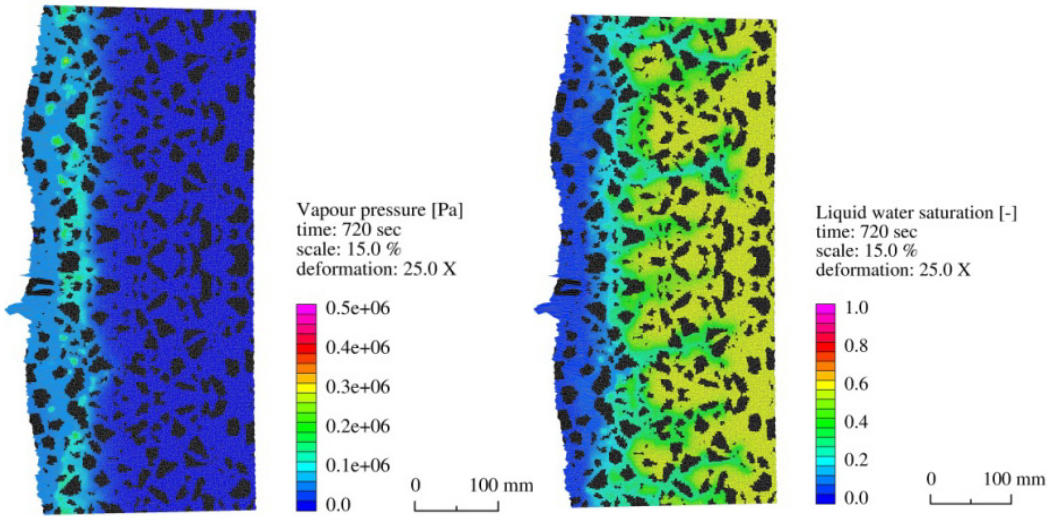

Figure 9: The level of cracking in especially the heated surface layer is sufficient to reduce the pore pressures, only representing a minor contribution to the local stress state (left). The increased drying rate also extends into the C25/30 cross-section along the cracks (right) (Lottman, 2017)

The influence of the crack pattern is also illustrated by the distribution of the liquid water saturation level in the right picture of figure 9. After 720 seconds the progress of the drying front is indicated to mainly correspond to the heated surface layer. The concrete dries faster, at lower temperatures and resulting pore pressures. Along cracks extending into the unheated part of the cross-section also some drying effects are observed. This is caused by the connectivity of these cracks to the exterior environment with the capillary pressure gradient driving the liquid water to the surface (Lottman, et al., 2015).

Drying of a cracked HSC cross-section by a standard fire scenario

The possibility for the pore pressure to still increase and attain values sufficient to contribute to fracture process is investigated subsequently by considering a High Strength Concrete (HSC) cross-section with a strength class C90/105. To further enhance the chance for the pore pressure to develop are the aggregate particles chosen as limestone which has a lower thermal expansion compared to the previously used river gravel (Eurocode 2, 2011b). This approach thus combines a higher tensile strength of the mortar and especially the interfacial transition zones with a reduction in the thermal loading.

By exposure of this cross-section to a HC fire scenario again severe cracking at the rear of the heated surface layer develops. This process did reflect a more moderate tendency in growth, but eventually the thermal stress gradient was sufficient to form the delamination process in the heated surface layer. The possibility to overcome the spalling mechanism was found to be a reduction in the imposed thermal loading. Figure 10 shows that exposure of C90/105 to a more moderate temperature development according to an ISO fire limits the level of cracking. This gives rise to pore pressure peaks which are however insufficient to cause the spalling mechanism.

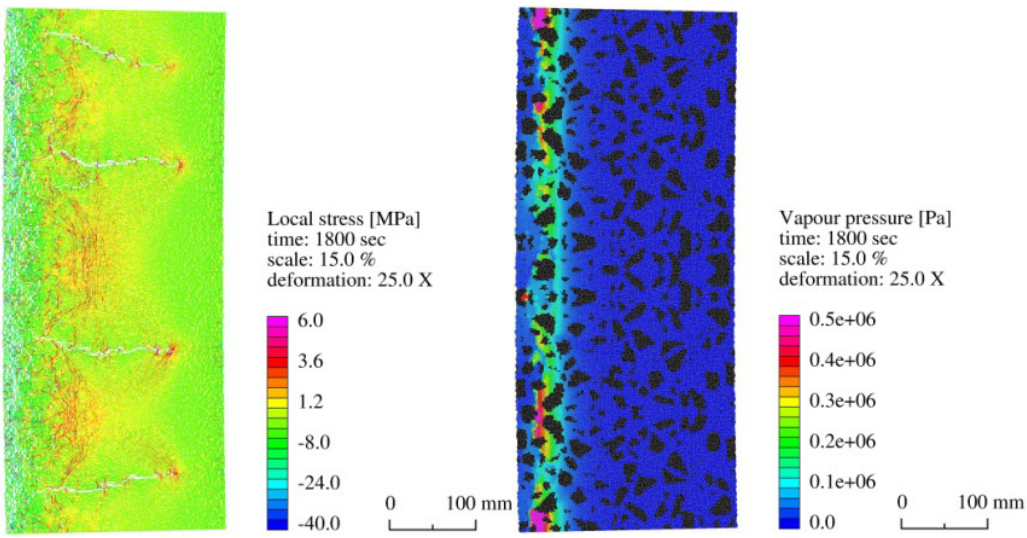

Figure 10: Drying of the C90/105 cross-section made with limestone aggregate during exposure to a more moderate ISO fire only reflects some localised pressure peaks (right). The level of damage in the surface layer is insufficient to cause the formation of unstable layers (left) (Lottman, 2017)

These and various other simulations discussed in (Lottman, 2017) seem to indicate that the contribution by the pore pressure to the local stresses is under these fire conditions limited, even compared to the relatively low tensile strength of NSC (RILEM TC-HTC, 2004). It also suggests that the possibility for the pore pressure to influence the formation of the thermal instabilities is to reach material with less cracks. This implies passing through the heated surface layer and develop in the cooler interior. However, this seems unlikely to occur since the process of forced drying and the pore pressure development are closely related to the temperature and thus will remain part of the heated surface layer (Lottman, 2017).

Measurement of pore pressures during full-scale testing

Finding evidence of pressure mitigation through cracking is difficult since mainly temperatures are measured during full-scale fire testing of concrete elements. However, some measurements of combined temperature and pressure acting at various depths in fire exposed concrete slabs are available and seem to confirm this tendency (Mindeguia, 2008; Jansson & Boström, 2008). Alternative collaboration for this behaviour can for instance be found by the reported spalling damage after fire exposure of an initially predried concrete slab loaded in compression (FSV, 2004). However, the absence of spalling has also been observed for similar slabs without the presence of external loading (Mindeguia, 2009). This latter difference is believed to indicate the need to consider the thermal stresses. More research into the impact of pre-drying the concrete on the mechanical properties is needed, considering for instance the formation of (micro) cracks and the influence on the ability to form and maintain the compressive restraining force in the heated surface layer.

8 Spalling mechanism of fire exposed concrete due to thermal buckling

The aspect reflected by the simulations and particular insightful with respect to spalling of fire exposed concrete is the formation of a surface-based failure mechanism (Lottman, 2017). Along the heated surface deformations were estimated to rapidly develop, originating from initial flaws already present after several minutes of fire exposure. Furthermore, these relatively thin layers reflected curvature shaped deformations due to, especially at the onset, compressive stress levels lower than the strength of the heated concrete. This combination could suggest that a form of thermal buckling occurs with the spalling mechanism governed by the compressive force reaching the critical buckling load (Timoshenko & Gere, 1961 / 2009). Sudden release of the remaining elastic energy is than the actual spalling event (FSV, 2004; Mindeguia, 2009).

Observations of the spalling mechanism

Evidence of this particular form of failure is for instance found in compressive cracks which by inclined propagation extend to the unheated part of the cross-section as shown in figure 11 by (Horvath, et al., 2004) and also observed by the first author after fire testing (Lottman, 2017). The simulated spalling mechanism can also be compared to for instance the distinctive crater shaped pockets observed for a loaded tunnel lining segment after full-scale fire testing, as shown in the right picture of figure 1 (Dehn, et al., 2010). However, the

tendency of the concrete to fail suddenly during fire exposure makes analysing the fracture process more difficult.

The premise of buckling also allows to argue that the fracture process of concrete under sudden thermal impact contributes to the seemingly random nature of spalling. The instability of layers at the heated concrete surface is based on the formed crack pattern, the thermally degraded stiffness of the concrete and especially the length. In retrospect it becomes clear that spalling can take various forms, reflecting dependence in observed time and sizes (FSV, 2004; Mindeguia, 2009). Similar discussions regarding the sensitivity to spalling of HSC and the negative influence of compression loading are reported in (Lottman, 2017).

Figure 11: Cracking of a HSC slab during thermal exposure according to the RWS fire curve (left) and resulting spalling damage (right) (Horvath, et al., 2004)

Thermal buckling of heated surface layers

The proposed spalling mechanism can be illustrated by the considering the deformation of the heated surface layer. The mechanical scheme seen in figure 12 reflects both the partially restrained expansion as well as the formation of a dominant crack, eventually separating part of the heated surface layer (Lottman, 2017). The continued fire exposure promotes the compressive force to develop with propagation of the crack reflected by additional curvature deformation. An elastic foundation of distributed translational springs are used to represent the resistance to crack formation. Additional aspects considered are the structural-based thermal curvature as well as an additional internal moment based on the change of the normal force centre (NC).

During outward curvature of this layer also horizontal forces develop which have to be resisted by the surrounding material. In case of NSC extensive cracking will have weakened this transition zone and eventually a curvature shaped fracture surface develops, indicating that failure through buckling occurs. In case of HSC a more uniform fracture surface develops which could explain the commonly reported sensitivity (Khoury & Anderberg, 2000).

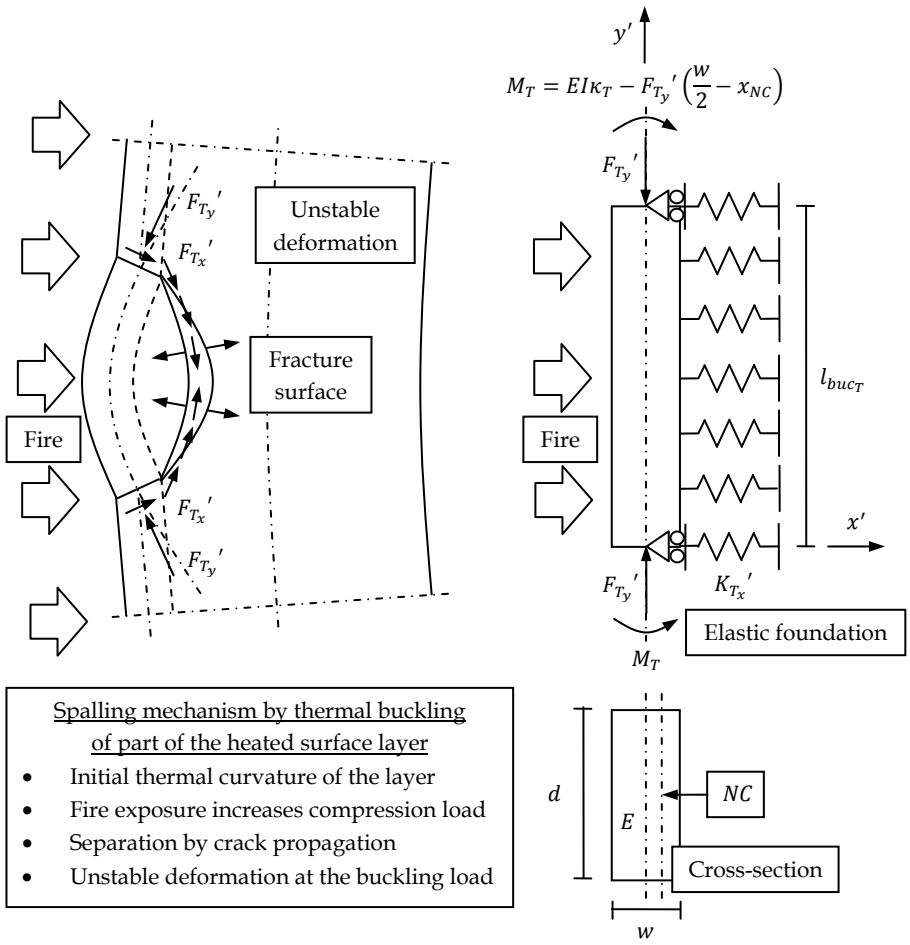

Figure 12: The spalling mechanism of fire exposed concrete by thermal-induced buckling of a heated surface layer until unstable deformations occur, proposed by (Lottman, 2017)

The statement of the critical buckling load thus depends on the geometrical properties of the layer which is formed in-time by the fracture process due to an increasing compressive force. However, it should be further noted that by using a plane strain assumption also in

the out-of-plane direction a restraining force develops. Under these circumstances the spalling mechanism reflects a plate loaded in bi-axial compression. Analysing this simplified buckling model could however prove very insightful.

Effectiveness of measures for spalling mitigation

Understanding the mechanism is the first step in reducing the sensitivity to spalling or alternatively the thermal buckling risk. The first possibility is to reduce the compressive load which can be achieved by the use of aggregates with a lower thermal expansion as for instance adopted by (FSV, 2004; Jansson & Boström, 2008; Dehn, et al., 2010). Another, less obvious possibility is to increase the level of cracking which in the simulations representing unrestrained slabs avoided the formation of the instabilities.

More of practical relevance to concrete structures are conditions with some level of restraint and possible external loading. Under these circumstances commonly fire protective measures such as boards or cladding are used. Reduction of the level of thermal exposure, for instance by project-based fire scenarios, could prove beneficial if allowed by the established provisions. Another possibility is the addition of polypropylene (PP) fibres to the concrete mixture (Horvath, et al., 2004; FSV, 2004). However, the limitation of pressures due to cracking raises the question of their effectiveness (Lottman, 2017). Extending on the concept of thermal buckling could suggest that the melting of the PP-fibres, commonly in the temperature interval of 160 °C to 170 °C (Brekelmans, et al., 2008), reduces the strength and stiffness of the concrete and thus the ability to sustain the thermal loading. More research is needed to validate this concept. However, it should be noted that without fire protection measures dehydration and thermal cracking of the concrete will still occur in these severe conditions.

9 Conclusions

In this article the derivation of a conceptual FEM-based model is presented in order to approximate both pore pressure and thermal stress development for a fire exposed concrete structural element. For this purpose two coupled FEM models are derived, having a heterogeneous and anisotropic basis.

The first FEM model describes the temperature and pore pressure development, characterising the mortar and interfacial transition zones by the process of forced drying

with the aggregates assumed impermeable. Boundary conditions reflect interaction with the surrounding environment. The second FEM model governs the thermal stresses development, including the influence of the pore pressure and is based on an anisotropic approximation of the global strains using three triangular orientated local strains. The structural behaviour is imposed by rigid bodies governed by coupling conditions.

The influence of the time-dependent crack development is included explicitly in both FEM models through coupling. The initiation and opening of the crack pattern is governed by a fracture mechanics approach based on brittle fracture commonly referred to as a lattice (Schlangen, 1993; Vervuurt, 1997). The local influence of cracks on the pore pressure development is reflected in the anisotropic definition of the water phase mass fluxes.

Based on several simulations, taken also from (Lottman, 2017), and by comparison with full-scale fire tests on concrete elements the following main conclusions are drawn:

- The influence of the temperature gradient is found to surpass the pore pressure. Simulations involving the process of forced drying indicate that the crack patterns formed by severe fire exposure are sufficient to reduce the pore pressures in both NSC as well as HSC. Under these circumstances is the contribution by the pore pressure to the local stresses considered to be minor.
- The progress of the drying front through the heated surface layer increases compared to non-cracked simulations, reflecting also drying along cracks extending into the cross-section. This latter effect is attributed to the capillary pressure gradient forcing the liquid water to flow towards the heated surface.
- For a hydrocarbon-based fire scenario the presence of structural restraint for the NSC and HSC element is of key importance. By addition of partial restraint the compressive stresses acting in the heated surface layer are conserved and eventually thermal instabilities at the heated surface are formed.
- The compressive stress level and the slenderness of these layers suggest that a form of thermal buckling occur. Various experimental results obtained from heated concrete samples and the observed damage after full-scale fire testing of concrete slabs is used to argue the validity of this premises.

10 Recommendations

The possibility provided by the FEM-based model to combine both existing theories on pore pressure development and temperature-induced stresses proofed particular valuable in assessing their contributions. Analysing these results and discussing their validity can therefore help to bridge the gap between experimental material-based research and full-scale fire testing. The findings presented and the possibilities to analyse the tendency for spalling of concrete elements can also be used to improve the fire safety design in practice as well as aid in improving the guidelines.

From the research work described the main recommendations are briefly given:

- The premise of thermal buckling allows to state a conceptual model, considering aspects such as the time-dependent compressive force, the structural level of restraint and the curvatures. This simplified model could form the starting point for further research.
- The FEM model should be further validated based on full-scale tests on concrete slabs in which temperature and preferably pore pressures as well as displacements are measured. Aspects to consider for numerical improvement are a higher order definition of the mass fluxes to enhance the pressure estimation along cracks as well as considering rotational equilibrium of forces to extend the definition of the anisotropic bars.

Acknowledgement
The authors like to thank the Netherlands Organisation for Scientific Research (NWO), formerly known as the Dutch National Science Foundation (STW), for financially supporting the research project on "Explosive spalling of concrete". This research project was a joint effort between Eindhoven University of Technology and Delft University of Technology and comprised of three PhD students.

Notations

General

A	[mm²]	Cross-sectional area defined perpendicular to an axis
t	[s]	Time or duration of fire exposure
l	[m], [mm]	Length defined parallel to an axis (based on ref. system)
Γ	[-]	Boundary of the discretised domain
Δ	[-]	Increment of a property
α	[rad]	Angle defined relative to a coordinate system
$\boldsymbol{n}$	[-]	Unit outward normal vector
$\boldsymbol{x}$	[m], [mm]	Coordinate system vector

$\ldots^{e}$	Indication for the element number
$\ldots^{e_d}$	Indication for edge 'd' of the triangular element
$\ldots^{I}, \ldots^{II}, \ldots^{III}$	Indications for the edges of the triangular element
$\ldots'$	Indication for a local definition
$\cdots_{i}$	Indication for the node number
$\cdots_{i_{rb}}$	Indication for the node number situated along the rigid body
$\cdots_{1}, \cdots_{2}, \cdots_{3}$	Indications for the nodes of the triangular element
$\cdots_{A}$	Indication for definition at the surface exposed to environment
$\cdots_{S}$	Indication for definition at a support
$\cdots_{T}, \cdots_{P}$	Indication for a contribution with respect to temperature, capillary pressure
$\cdots_{U}$	Indication for the variables, horizontal and vertical displacements
$\cdots_{U_M}, \cdots_{U_G}$	Indication for a material, geometrical contribution with respect to the horizontal and vertical displacements
$\ldots^{t}$	Indication for the incremental time step
$\cdots_{k}$	Indication for the incremental (crack) step
$\cdots_{rb}$	Indication for definition at the rigid body boundary condition

$\overline{\cdots}$	Indication for an averaged definition
$\underline{\cdots}$	Indication for a tensor property
$\cdots_{\infty}$	Indication for definition of a property at distance from the surface

Temperature and pore pressure

C	[J/kgK]	Specific heat capacity of the material
H_{vap}	[J/kg]	Enthalpy of vaporization per unit of mass
K_{cr}	[m²]	Permeability defined by opening of the crack
K_{rel_g}, K_{rel_w}	[-]	Relative permeability of the gas, liquid phase
K_{xx}, K_{yy}	[m²]	Principal directions of permeability
M_w	[kg/mol]	Molar mass of water defined as 0.018015 kg/mol
P_C	[Pa]	Capillary pressure acting between the water phases
P_{gw}	[Pa]	Partial pressure of water vapour in the gas phase
P_{sat}	[Pa]	Saturated water vapour pressure
P_w	[Pa]	Pressure of the liquid phase
R	[J/molK]	Universal gas constant defined as 8.3144 J/molK
RH	[-]	Relative humidity of the material
S_w	[-]	Saturation level of the liquid phase
T	[K]	Temperature
n	[-]	Porosity of the material
w	[m]	Crack width
α_A	[W/m²K]	Convective heat transfer coefficient of the material
β_A	[m/s]	Convective mass transfer coefficient of the material
μ_g, μ_w	[kg/ms]	Dynamic viscosity of the gas, liquid phase
ρ	[kg/m³]	Density of the material
ρ_{gw}, ρ_w	[kg/m³]	Density of the water vapour, liquid water phase
ρ_{vap}	[kg/m³]	Mass density of water vapour due to evaporation
$\boldsymbol{q_{gw}}, \boldsymbol{q_w}$	[kg/m²s]	Mass flux vector of water vapour, liquid water
$\boldsymbol{q_T}$	[J/m²s]	Heat flux vector of thermal energy

$\boldsymbol{K}$	[m²]	Permeability tensor (second order)
$\boldsymbol{T_\alpha}$	[-]	Coordinate transformation tensor (second order)
$\boldsymbol{k}$	[W/mK]	Thermal conductivity tensor (second order)

Fracture mechanics

E	[MPa]	Young's modulus of the material
d_{rel}	[mm]	Distance along the edge relative to the support
d_{rel_T}	[mm]	Temperature elongation defined relative to the support
u_x, u_y	[mm]	Horizontal, vertical displacement
ε	[-]	Total extensional strain
ε_T	[-]	Temperature-induced elongation strain
$\varepsilon_{xx}, \varepsilon_{yy}$	[-]	Extensional strain acting along the x-axis, y-axis
γ_{xy}	[-]	Shearing strain
ν	[-]	Poisson's ratio of the material
σ	[MPa]	Stress
σ_p	[MPa]	Pressure-induced stress
σ_{xx}, σ_{yy}	[MPa]	Extensional stress acting along the x-axis, y-axis
σ_{xy}	[MPa]	Shear stress
φ	[rad]	Rotation
$\boldsymbol{F_S}$	[var.]	External load defined as force vector at the support
$\boldsymbol{f}$	[MPa]	Body force vector
$\boldsymbol{u}$	[mm]	Displacement vector
$\boldsymbol{u_T}$	[mm]	Displacement vector based on the temperature strain
$\boldsymbol{\varepsilon}$	[-]	Total strain vector
$\boldsymbol{\varepsilon_T}$	[-]	Temperature-induced strain vector
$\boldsymbol{\sigma}$	[MPa]	Stress vector
$\boldsymbol{\sigma_P}$	[MPa]	Pressure-induced stress vector

$\boldsymbol{B}$	[1/mm]	Gradient matrix of linear shape functions
$\boldsymbol{C}$	[MPa]	Elasticity tensor (fourth order)
$\boldsymbol{D}$	[MPa]	Elasticity tensor using engineering notation (fourth order)
$\boldsymbol{K_S}$	[var.]	Spring stiffness matrix governing the structural interaction
$\boldsymbol{T_{rb}}$	[var.]	Transformation tensor based on coupling conditions along the rigid body edge (second order)
$\boldsymbol{T_\varepsilon}$	[-]	Strain transformation tensor (fourth order)
$\underline{\boldsymbol{\varepsilon}}$	[-]	Total strain tensor (second order)
$\underline{\boldsymbol{\sigma}}$	[MPa]	Stress tensor (second order)

References

Alonso, C. & Fernandez, L., 2004. Dehydration and rehydration processes of cement paste exposed to high temperature environments. *Journal of materials science,* 39(9), pp. 3015-3024.

Bachmat, Y. & Bear, J., 1986. Macroscopic modelling of transport phenomena in porous media 1: the continuum approach. *Transport in Porous Media,* 1(3), pp. 213-240.

Bathe, K. J., 1986. *Lecture notes - finite element procedures for solids and structures, non linear analysis (reorder nr. 73-2200).* Cambridge, United States of America: Department of Mechanical Engineering - Massachusetts Institute of Technology.

Bear, J., 1972/1988. *Dynamics of fluids in porous media.* New York, United States of America - New York, United States of America: Original published by American Elsevier Publishing Company, Inc. - republished by Dover Publications, Inc..

BEA-TT & RAIB, 2010. *Technical investigation report concerning the fire on Eurotunnel freight shuttle 7412 on 11 September 2008.* La Défense cedex, Paris, France / Derby, United Kingdom: Bureau d'enquêtes sur les accidents de transport terrestre / Rail Accident Investigation Branch.

Blaauwendraad, J., 2004. *Lecture notes CT3130 - plates and slabs, volume 2: numerical methods.* Delft, the Netherlands: Faculty of Civil Engineering and Geosciences - Delft University of Technology.

Blom, C. B. M., 2009. *Practical FEM program coding.* Delft, the Netherlands: Concept.

Bouma, A. L., 2000. *Mechanica van Constructies: elasto-statica van slanke structuren (in Dutch).* Delft, the Netherlands: Delft University Press.

Brekelmans, J. W. P. M., Breunese, A. J. & Vervuurt, A. H. J. M., 2008. *TNO report - Research on spalling of concrete during fire - 2007-D-R1329/B - part 1: test set-up, 2007-D-R1330/B - part 2: preparation of test specimen, 2007-D-R1331/B - part 3: fire tests, 2007-D-R1332/B - part 4: analysis.* Delft, the Netherlands: TNO Built Environment and Geosciences.

CTSA, 1997. *Inquiry into the fire on Heavy Goods Vehicle shuttle 7539 on 18 November 1996.* London, United Kingdom: Channel Tunnel Safety Authority.

Dehn, F. et al., 2010. *Bast Heft B73 - Brand- und Abplatzverhalten von Faserbeton in Straβentunneln (in German) - Gesellschaft für Materialforschung und Prüfungsanstalt für das Bauwesen, Leipzig, Germany.* Bergisch Gladbach, Germany: Bundesanstalt für Straβenwesen.

Dougill, J. W., 1972. Modes of failure of concrete panels exposed to high temperatures. *Magazine of Concrete Research,* 24(79), pp. 71-76.

Eurocode 1, 2011a. *Actions on structures - part 1-2: General actions - actions on structures exposed to fire - NEN-EN 1991-1-2+C1: 2011 - NL version (in Dutch).* Brussels, Belgium: European Committee for Standardization.

Eurocode 2, 2011b. *Design of concrete structures - part 1-2: General rules - structural fire design - NEN-EN 1992-1-2+C1:2011 - NL version (in Dutch).* Brussels, Belgium: European Committee for Standardization.

Felippa, C. A., 2004a. *Lecture notes course ASEN 5007 - introduction to finite element methods.* Boulder, United States of America: Department of Aerospace Engineering Sciences and Center for Aerospace Structures - University of Colorado.

fib WP-4.3-1, 2007. *Fire design of concrete structures: materials, structures and modelling - Working Party, state of art report.* Lausanne, Switzerland: International Federation for Structural Concrete (fib).

FSV, 2004. *Brandbeständigkeit von Faser-, Stahl- und Spannbeton - Schriftenreihe Straβenforschung - heft 544 (in German).* Vienna, Austria: Österreichische Forschungsgemeinschaft Straβe und Verkehr, Republik Österreich, Bundesministerium für Verkehr, Innovation und Technologie, Bundesstraβenverwaltung.

Gavin, H. P., 2014. *Lecture notes course CEE 421L - matrix structural analysis, geometric stiffness effects in 2D trusses.* Durham, United States of America: Department of Civil and Environmental Engineering - Duke University.

Gawin, D., Pesavento, F. & Schrefler, B. A., 2003. Modelling of hygro-thermal behaviour of concrete at high temperature with thermo-chemical and mechanical material

degradation. *Computer Methods in Applied Mechanics and Engineering,* 192(13-14), pp. 1731-1771.

Genuchten, M. T., 1980. A closed form equation for predicting the hydraulic conductivity of unsaturated soils. *Soil Science Society of America Journal,* 44(5), pp. 892-898.

Gray, W. G. & Schrefler, B. A., 2001. Thermodynamic approach to effective stress in partially saturated porous media. *European Journal of Mechanics - A/Solids,* 20(4), pp. 521-538.

Harmathy, T. Z., 1965. Effect of moisture on the fire endurance of building materials. *ASTM Special Technical Publication 385,* pp. 74-95.

Hartmann, F. & Katz, C., 2007. *Structural analysis with finite elements.* Berlin Heidelberg, Germany: Springer-Verlag.

Hartsuijker, C. & Welleman, J. W., 2007. *Engineering mechanics - volume 2 - stresses, strains, displacements.* Dordrecht, the Netherlands: Springer.

Hassanizadeh, M. & Gray, W. G., 1979a. General conservation equations for multi-phase systems 1: averaging procedure. *Advances in Water Resources,* Volume 2, pp. 131-144.

Hassanizadeh, M. & Gray, W. G., 1979b. General conservation equations for multi-phase systems 2: mass, momenta, energy and entropy equations. *Advances in Water Resources,* Volume 2, pp. 191-203.

Horvath, J., Schneider, U. & Diederichs, U., 2004. *Heft 11 - Beiträge zum Abplatzverhalten von Hochleistungsbetonen (in German).* Vienna, Austria: TU Vienna, Institute for Building Materials, Buildings Physics and Fire Protection.

Jansson, R. & Boström, L., 2008. *SP report 2008:52 - Spalling of concrete exposed to fire.* Borås, Sweden: SP Technical Research Institute of Sweden.

Khoury, G. A., 2008a. Passive fire protection of concrete structures. *Structures & Buildings,* 161(3), pp. 135-145.

Khoury, G. A. & Anderberg, Y., 2000. *Fire Safety Design - concrete spalling review.* Sweden: Report submitted to the Swedish National Road Administration.

Kordina, K., 1963. *Heft 2 - Das Verhalten von Stahlbeton- und Spannbetonbauteilen unter Feuerangriff (in German).* Braunschweig, Germany: Institut für Baustoffkunde und Stahlbetonbau der Technischen Hochschule Braunschweig.

Lottman, B. B. G., 2017. *The spalling mechanism of fire exposed concrete.* Delft, the Netherlands: PhD thesis TU Delft.

Lottman, B. B. G., Koenders, E. A. B., Blom, C. B. M. & Walraven, J. C., 2013. *Spalling of concrete due to fire exposure: a coupled fracture mechanics and pore pressure approach.* Paris,

France, Proceedings of the 3rd International Workshop on Concrete Spalling due to Fire Exposure.

Lottman, B. B. G., Koenders, E. A. B., Blom, C. B. M. & Walraven, J. C., 2015. *Spalling of fire exposed concrete based on a coupled material description: an overview.* Leipzig, Germany, Proceedings of the 4th International Workshop on Concrete Spalling due to Fire Exposure.

Lottman, B. B. G., Koenders, E. A. B. & Walraven, J. C., 2011. *Macro-scale spalling model: a fracture mechanics versus pore pressure approach.* Delft, the Netherlands, Proceedings of the 2nd International RILEM Workshop - Concrete Spalling due to Fire Exposure.

Lottman, B. B. G. et al., 2017. Spatmechanisme bepalend voor brandveiligheid tunnels (in Dutch). *Cement,* Issue 8, pp. 26-35.

Mindeguia, J. C., 2008. *Caractérisation thermo-hydrique et comportement au feu de deux bétons: analyse des risques d'instabilités (in French).* Nancy, France, Proceedings of the 26th Rencontres Universitaires de Génie Civil.

Mindeguia, J. C., 2009. *Contribution expérimentale a la compréhension des risques d'instabilité thermique des bétons (in French).* Pau, France: PhD thesis l'université de Pau et Pays de L'Adour.

Pel, L. & Huinink, H., 2007. *Lecture notes course 3F250 - Transport in porous media.* Eindhoven, the Netherlands: TU Eindhoven, Department of Applied Physics.

Prezemieniecki, J. S., 1968/1985. *Theory of matrix structural analysis.* New York, United States of America - New York, United States of America: Original published by McGraw-Hill Book Company, Inc. - republished by Dover Publications, Inc..

RILEM TC-HTC, 2004. *Behaviour of concrete at high temperatures - Technical Committee, state of art report - part 1 - ordinary concrete.* Bagneux, France: RILEM publications S.A.R.L..

RWS, 2017. *Richtlijnen Ontwerp Kunstwerken - ROK versie 1.4 (in Dutch).* Utrecht, the Netherlands: Rijkswaterstaat Grote Projecten en Onderhoud.

Schlangen, E., 1993. *Experimental and numerical analysis of fracture processes in concrete.* Delft, the Netherlands: PhD thesis TU Delft.

Segal, A., 2008. *Lecture Notes J.M. Burgerscentrum, Research School for Fluid Mechanics - finite element methods for the incompressible Navier-Stokes equations.* Delft, the Netherlands: Faculty of Electrical Engineering, Mathematics and Computer Science - Delft University of Technology.

Söderlind, G. & Wang, L., 2006. Adaptive time-stepping and computational stability. *Journal of Computational and Applied Mathematics,* 185(2), pp. 225-243.

Spencer, A. J. M., 1980/2004. *Continuum mechanics.* Essex, United Kingdom - New York, United States of America: Original published by Longman Group UK limited - republished by Dover publications, Inc..

Tenchev, R. T., Li, L. Y. & Purkiss, J. A., 2001. Finite element analysis of coupled heat and moisture transfer in concrete subjected to fire. *Numerical Heat Transfer, Part A: Applications,* 39(7), pp. 685-710.

Timoshenko, S. P. & Gere, J. M., 1961/2009. *Theory of elastic stability, second edition.* New York, United States of America and London, United Kingdom - Minealo, New York, United States of America: Original published by McGraw-Hill Book Company, Inc. - republished by Dover publications, Inc..

Timoshenko, S. P. & Goodier, J. N., 1970. *Theory of Elasticity.* Singapore: Mcgraw-Hill Book Company.

van Breugel, K., Braam, C. R., van der Veen, C. & Walraven, J. C., 1998. *Betonconstructies onder temperatuur- en krimpvervormingen BP2 (in Dutch).* Boxtel, the Netherlands: Aeneas.

van Kan, J., Segal, A. & Vermolen, F., 2008. *Numerical methods in scientific computing.* Delft, the Netherlands: VSSD.

Vervuurt, A. H. J. M., 1997. *Interface fracture in concrete.* Delft, the Netherlands: PhD thesis TU Delft.

Wells, G. N., 2006. *Lecture notes course CT5123 - the finite element method: an introduction.* Delft, the Netherlands: Faculty of Civil Engineering and Geosciences - Delft University of Technology.

Zienkiewicz, O. C., Taylor, R. L. & Zhu, J. Z., 2005. *The finite element method: its basis and fundamentals (sixth edition).* Oxford, United Kingdom: Elsevier Butterworth-Heinemann.